Journal of
Materials Chemistry B

PAPER

View Article Online
View Journal | View Issue

Cite this: *J. Mater. Chem. B*, 2022, **10**, 1301

Highly stretchable, self-healable, and self-adhesive ionogels with efficient antibacterial performances for a highly sensitive wearable strain sensor†

Haibo Wang,[ab] Junhuai Xu,*[a] Kaijun Li,[a] Yi Dong,*[a] Zongliang Du[a] and Shuang Wang[ab]

Received 7th January 2022,
Accepted 24th January 2022

DOI: 10.1039/d2tb00041e

rsc.li/materials-b

Gel-based strain sensors with multi-functional outstanding properties have gained considerable attention. However, conventional gel sensors suffer from unsatisfactory mechanical properties and adhesion, and also a lack of self-healing and antibacterial ability. Herein, a multi-functional ionogel has been constructed based on Ag-Lignin nanoparticles (Ag-Lignin NPs), polyurethane (PU), and ionic liquids. The obtained ionogel exhibited excellent mechanical properties (tensile strength: 3.14 MPa, elongation at break: 1241%), and was conferred self-healing ability by introducing the disulfide bonds into the main chain (the best self-healing efficiency is 97.6%). The dynamic catechol redox system based on Ag-Lignin NPs endows the ionogel with repeatable and long-lasting adhesiveness. Besides, the obtained ionogel also presented favorable antibacterial and UV absorption properties. The sensor based on the ionogel possesses good and stable sensing performance. This study proposes a bright new strategy to fabricate multi-functional ionogel-based sensors exerting broad application prospects in the field of human movement and personalized physiological health monitoring.

Introduction

Ionic skin, which is believed to be the most attractive candidate to mimic human skin, is receiving considerable attention in applications.[1–6] In general, numerous hydrogels can serve as ideal ionic skin due to their transparency, stretchability, and excellent sensitivity. However, the intrinsic drawback of hydrogels, such as the low environmental stability, limited their application in wearable sensors. Compared with traditional hydrogels, ionogels, which were composed of a polymer network and numerous ionic liquids (ILs), are more suitable to adapt to harsh environments.[7–10] ILs possess not only excellent ionic conductivity and thermal stability but also strong interaction with polymer chains. Therefore, it is a promising strategy to design ionogels as flexible strain sensors for long-term application. Nevertheless, ionogel-based sensors usually suffer from low stretchability and fatigue resistance and are easily broken during deformation.

Polyurethane elastomers, with high strength and excellent toughness, have been widely used in wearable electric devices, electric skins, and flexible sensors. The combination of ILs and polyurethane could generate ionogels and serve as flexible strain sensors.[11–14] Gou *et al.* reported a supramolecular ionogel with high mechanical performance, which is fabricated by an amphiphilic poly(urethane-urea) copolymer and IL.[15] Furthermore, the results demonstrated that the mechanical properties have been enhanced after introducing lignin into the PU prepolymer.[16–18] The main reason is that lignin can act as hard segments and hard crosslinking points, leading to improved mechanical stiffness. Therefore, the mechanical properties of PU-based gels would be greatly enhanced *via* introducing crosslinking points.

Self-healable materials are regarded as one of the finest solutions to the challenge of the durability of ionic skins, which can recover mechanical damage. Numerous polymer materials have been successfully designed with self-healing abilities to enhance durability and prolong the service life. The healing behavior can be realized autonomously through the reversibility of dynamic covalent bonds.[19,20] Due to the low bond energy of disulfide bonds, the broken disulfide bonds would facilely re-form in mild conditions. It is this facile reversible transformation that has led to the widespread application of disulfide bonds in the design of self-healing materials. Additionally, the

---

[a] *College of Biomass Science and Engineering, Sichuan University, Chengdu 610065, P. R. China. E-mail: xujunhuaiup@163.com, waydongyi2501779@163.com*
[b] *The Key Laboratory of Leather Chemistry and Engineering of Ministry of Education, Sichuan University, Chengdu 610065, P. R. China*

† Electronic supplementary information (ESI) available: Additional figures as described in the text. See DOI: 10.1039/d2tb00041e

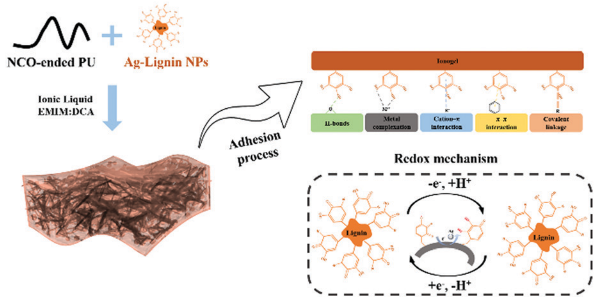

Fig. 1 Design strategy and mechanism of the self-adhesive ionogel.

efficiency and convenience of its use as a self-healing moiety have been demonstrated in multiple studies.[21–23]

In addition, the adhesion properties of ionic skins have proven to be of great importance in previous studies. However, the ionic liquids usually lack enough interfacial adhesion with substrates. Therefore, the introduction of long-lasting adhesion mechanisms in ionic skins has become an important challenge. Chen *et al.* imparted excellent long-lasting adhesion properties by introducing Ag-TA nanoparticles into the hydrogel.[24] The main mechanism is the continuous regeneration of catechol groups through the redox reaction of metal ions with TA, and a similar mechanism has been proved in other studies.[25–30]

To address the issues mentioned above, we have employed an isocyanate-capped polyurethane prepolymer and Ag-Lignin nanoparticles to obtain a cross-linked structure and then evaporate in ionic liquids to produce an ionogel (Fig. 1). The introduction of Ag-Lignin nanoparticles and carboxyl groups would extensively enhance the adhesive performance, and the hard cross-linked effect of the nanoparticles would endow the ionogel with improved mechanical properties. The self-healing capability can be acquired through the introduction of disulfide bonds in the main chains. Most importantly, the favorable compatibility of the ILs with polymers allows the free movement of ions in the ionogel, which will confer good electrical conductivity to the obtained ionogel, providing stable generation of sensing signals.

Experiments

Materials

1-Ethyl-3-methylimidazolium dicyanamide (EMIM:DCA) was purchased from Lanzhou Greenchem ILs (LICP, CAS). Poly(propylene glycol) (PPG_{2000}), $AgNO_3$, lignin, dibutyltin dilaurate (DBTDL), isophorone diisocyanate (IPDI), 4-aminophenyl disulfide and 2,2-bis(hydroxymethyl)propionic acid (DMPA) were purchased from Aladdin Reagent (Shanghai) Co., Ltd. If not particularly indicated, all other reagents were obtained from KeLong Reagent (Chengdu) Co., Ltd and used without further purification.

Preparation of Ag-Lignin nanoparticles (Ag-Lignin NPs)

The Ag-Lignin NPs were synthesized *via* the method reported in our previous study.[30] The aqueous solution of lignin was first prepared by dissolving the lignin powder in a NaOH solution. Then, the resulted solution was slowly added to the $[Ag(NH_3)_2]^+$ solution and reacted for 1 h at room temperature. The reaction between lignin and $[Ag(NH_3)_2]^+$ solution was analyzed by the CV test. DLS, FT-IR, XPS, and XRD were also used to determine the successful preparation of Ag-Lignin NPs.

Synthesize of cross-linked PU containing disulfide bonds (ALP)

A PPG, DMPA and IPDI were reacted in DMF in the presence of the catalyst for 4 h, and then 4-aminophenyl disulfide was used to extend the chain for 1 h to obtain an NCO-capped polyurethane prepolymer. Then, well-dispersed Ag-Lignin NPs were added into the above solution, and stirred for another 2 h (Fig. S1, ESI†) (the weight- and number-average molecular weights of NCO capped polyurethane prepolymer was determined to be around 14.2 kDa and 8.6 kDa by GPC, and the corresponding polydispersity (PDI, M_w/M_n) was 1.34).

Preparation of ionogels (ALP-I_x)

A fixed amount of the ALP solution was mixed with different contents of EMIM:DCA (0 wt%, 10 wt%, 20 wt%, and 30 wt%), denoted as ALP-I_0, ALP-I_1, ALP-I_2, ALP-I_3, respectively. The mixture was disposed on a mould placed at room temperature for 48 h, and then at 60 °C for 24 h to completely evaporate the solvent.

Results and discussion

Fabrication and characterization of ionogels

Ag-Lignin NPs were first prepared through a redox reaction. The quinone-catechol reversible reaction can be realized by the Ag-Lignin NPs, which would endow the ionogel with a long-lasting adhesion ability. In addition, the cyclic voltammetry (CV) experiments and XPS were used to demonstrate this process (Fig. 2a). A prominent redox peak at 0.10–0.20 V is presented in the curve of CV scanning, which can be attributed to the quinone reduction and catechol oxidation.[29,30] The XPS results demonstrate that lignin possessed a low content of C═O

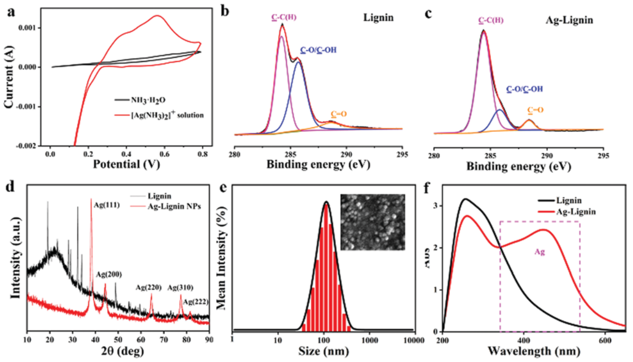

Fig. 2 Characterizations of the Ag-Lignin NPs: (a) CV curves of the $[Ag(NH_3)_2]^+$ solution; (b and c) XPS spectra in the C 1s regions of Lignin and Ag-Lignin; (d) XRD patterns of the Lignin and Ag-Lignin; (e) DLS analysis of the Ag-Lignin and SEM photo of Ag-Lignin NPs; (f) UV-vis spectra of Lignin and Ag-Lignin.

(288.4 eV) and high contents of C–OH and C–O (285.7 eV). However, the content of C=O sharply increases and the contents of C–OH and C–O greatly decrease after lignin reacted with $[Ag(NH_3)_2]^+$ (Fig. 2b and c). The Ag peak that appears in the XRD spectrum demonstrated that Ag was converted from Ag^+ by the redox reaction (Fig. 2d). SEM micrograph reveals the particle structure of Ag-Lignin NPs (inset in Fig. 2e). The DLS analysis determined the average size of the Ag-Lignin NPs to be around 120 nm (Fig. 2e). UV-Vis spectra analysis reveals the surface plasmon resonance of Ag-Lignin NPs. As presented in Fig. 2f, the appearance of the enhanced quadrupole plasmon resonance emerges in the region of 400 nm–500 nm after the addition of Ag.

Then, the well-prepared ionogel is confirmed by the FT-IR spectrum. The comparison spectra of Lignin, Ag-Lignin NPs, IL, PU, and ALP-I_2 are displayed in Fig. S2 (ESI†). Compared with the spectra of lignin and Ag-Lignin, the peaks at 2840 cm^{-1} (a symmetric stretch for $-CH_3$) and 1217 cm^{-1} (the syringyl ring breathing with C–O stretching) of Ag-Lignin are decreased or disappeared, which proves that the methoxy groups were oxidized by silver. In addition, bands that appear at 1656 and 1774 cm^{-1} are assigned to the stretching vibrations of C=O. The characteristic peaks of EMIM:DCA located at 2226 cm^{-1}, 2191 cm^{-1}, and 2124 cm^{-1} are assigned to the symmetric and asymmetric stretching vibrations of the C≡N bonds. After the Ag-Lignin NPs and PU composited in ILs, the peaks of Ag-Lignin NPs and ILs appear in the spectrum of ALP-I_2, and the peak of NCO groups (2280 cm^{-1}) disappeared, indicating that the prepolymer was well cross-linked by the lignin. The analysis of the FT-IR spectra above demonstrates that the cross-linked ionogel has been successfully synthesized.

Mechanical properties of ionogels

Benefiting from the cross-linked PU network, strong H-bonding character of the multi-urea and the reinforcement of the nanoparticles can form strong nanodomains and lead to excellent mechanical properties. To quantitatively determine the mechanical properties of the ionogels, a series of tensile tests were conducted. For different IL contents, ionogels exhibited different mechanical properties. The elongation at break of ionogels fluctuates from 893 to 1241%, and the tensile strength (4.99 to 0.49 MPa) and Young's modulus (1.71 to 0.35 MPa) gradually decrease with the addition of IL, respectively (Fig. 3a, the detailed data are listed in Table 1). Such a phenomenon can be attributed to the plasticizing effect of IL on PU. Due to the excellent solubility of IL, the crystalline region, and nanoparticles in the microphase separation are partially dissolved, resulting in the decrease of tensile strength and Young's modulus. Moreover, the dissolution of a small part of the crystalline zone led to the extension of the PU chains, which increases the elongation at break. However, with the excessive dissolution of the crystalline zone (extensive IL additions), the tensile strength and the elongation at break dramatically decreases. Besides, as shown in Fig. 3b, ten cycles of stretching test at 200% strain were investigated (ALP-I_2), and a residual strain of 18% is exhibited after the first stretching cycle.

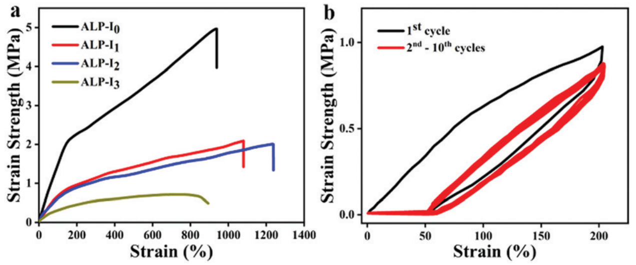

Fig. 3 Mechanical properties of ionogel: (a) the tensile stress–strain curves of the ionogel with different IL addition; (b) 10 times repeated strain curve at 200%.

Table 1 The detailed data of mechanical properties

Samples	Strength (MPa)	Elongation at break	Young's modulus (MPa)
ALP-I_0	4.99	976	1.71
ALP-I_1	2.09	1078	1.15
ALP-I_2	2.01	1241	0.91
ALP-I_3	0.49	893	0.35

The next nine stretching curves are well duplicated with negligible hysteresis loops. The exceptional tensile performance of the prepared ionogel fully demonstrates its potential in flexible materials applications. Based on the above-mentioned results, ALP-I_2 was selected as the sample for the next studies due to its excellent mechanical properties.

Self-healing properties of ionogels

Owing to the large number of reversible disulfide bonds, ionic bonds, and hydrogen bonds in the ionogel, ALP-I_2 is supposed to present great self-healing property. The self-healing mechanism is illustrated in Fig. 4a, which can be attributed to the re-form of the disulfide bonds, ionic bonds, and hydrogen bonds in the ionogel. First, the self-healing process was observed by POM with a heat stage (Fig. 4b). The scratch disappeared after heating at 50 °C for 60 min. To qualitatively study the self-healing property of ALP-I_2, the sheared ALP-I_2 was reattached together in an oven at 50 °C healing for 60 min. Unsurprisingly, the self-healed ALP-I_2 can be stretched for several times to the original length without any fracture (Fig. 4c). The mechanical properties of ALP-I_2 for different self-healing time periods were also explored to quantitatively analyze its self-healing property. As depicted in Fig. 4d, e, the self-healing efficiency of ALP-I_2 increases significantly with the increase in the self-healing time (room temperature and heated condition). The effect is more effective under heated conditions, and the best healing efficiency is 97.6% (healed for 60 min at 50 °C). The healing efficiency is only 85.2% after 24 h of self-healing at room temperature.

Self-adhesive properties of ionogels

Currently, due to the poor fit between the sensor and human skin, the detection data of the mechanical sensor are usually biased. Therefore, sufficient adhesion between the sensor and human skin must be guaranteed to ensure accurate monitoring.

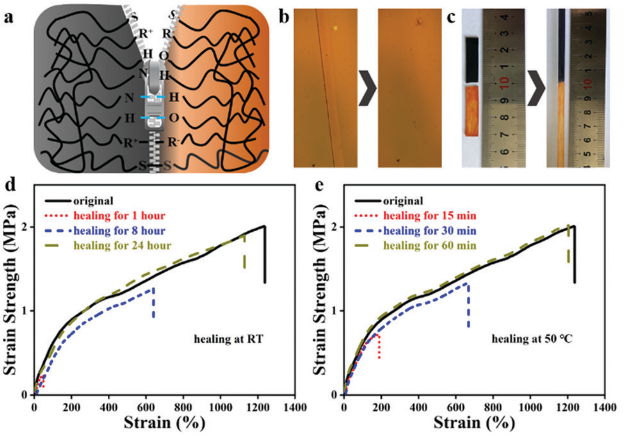

Fig. 4 Self-healing properties of the ionogel: (a) illustration of the self-healing mechanism; (b) POM photos of the ionogel before and after self-healing; (c) qualitative tensile photos of ionogel before and after self-healing; (d and e) the tensile curves of the ionogel healing at room temperature or 50 °C for different time.

Ag-Lignin NPs were demonstrated to endow the gel with outstanding adhesion.[31] Owing to the continuously generated catechol groups *via* the process of a dynamic redox reaction, the composite gels could attach tightly to various substrates by covalent and noncovalent bonding. Consequently, the ionogel that we prepared presents superior and repeatable adhesiveness to different substrates (Fig. 5a). The tensile adhesion test was utilized to quantitatively determine the adhesion strength of the ionogel on different surfaces. As shown in Fig. 5b, the adhesion strengths to plastic, glass, PTFE, and hogskin are 22.6, 19.7, 10.41, and 8.1 kPa, respectively. Besides, the repeated peeling/adhering cycle was also studied. The ionogel maintained great adhesion (84.1%) after 6 cycles (Fig. 5c). The remarkable adhesiveness of the ionogel is mainly assigned to the effect of catechol groups of Ag-Lignin NPs in the ionogel. The redox system constructed by the Ag-Lignin NPs supports the reversible switching between quinone and catechol groups. The catechol groups and methoxy groups on the lignin can be oxidized to quinone/hydroquinone, while these groups will be converted into catechol groups again by the photogenerated electrons (electrons can be generated by the AgNPs). In contrast, an ionogel without Ag-Lignin NPs did not exhibit repeatable adhesion due to the absence of the redox environment. In brief, the adhesion of the ionogel contained Ag-Lignin NPs will be guaranteed by the redox process.

Anti-freezing, UV-shielding, and anti-bacterial properties of ionogels

To monitor human movements, the sensor will often be exposed to some extreme environments, such as sub-zero temperature. Therefore, the anti-freezing properties of the sensor appear to be particularly important. To verify the anti-freezing capability of the obtained ionogel, DMA measurement was utilized to determine the information on storage modulus and loss factor of ALP-I_2 in the range from −80 °C to 120 °C. As presented in Fig. 6a, the storage modulus decreases dramatically at first and then remains constant with the increase in temperature. The loss factor indicates a glass transition temperature of −41.6 °C. The low T_g implies that the excellent tensile properties of the ionogel could be preserved at a low temperature. Besides, various tensile tests were conducted on ALP-I_2 at different temperatures (Fig. 6b). The strain strength and elongation at the break of the ionogel before and after the treatment remain virtually unchanged, indicating that the ambient temperature has no obvious effect on the mechanical properties of ionogel. The ionogel can be stretched several times to the original at −20 °C for 1 day storage, which further supports the anti-freezing ability of the ionogel (the inset picture of Fig. 6b). Moreover, the weight of the samples hardly changed even after being placed in a dry fume hood for 20 days (Fig. S3, ESI†), indicating that the obtained ionogel has excellent thermal stability and anti-volatility properties.

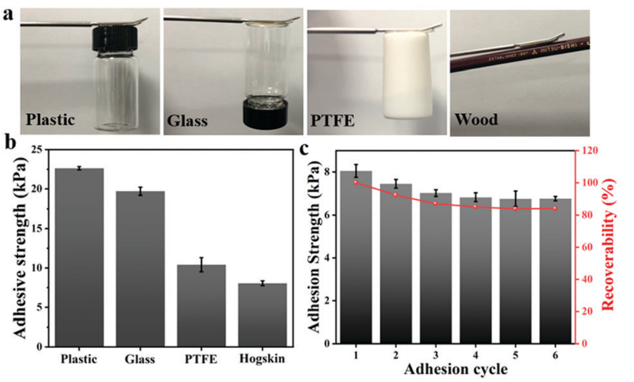

Fig. 5 The adhesion properties of the ionogel: (a) photos of the ionogel on the surface of various substrates including plastic, glass, PTFE, and wood; (b) quantification of the adhesion of ionogels to different object surfaces; (c) repeatable adhesion behavior of the ionogel to hogskin.

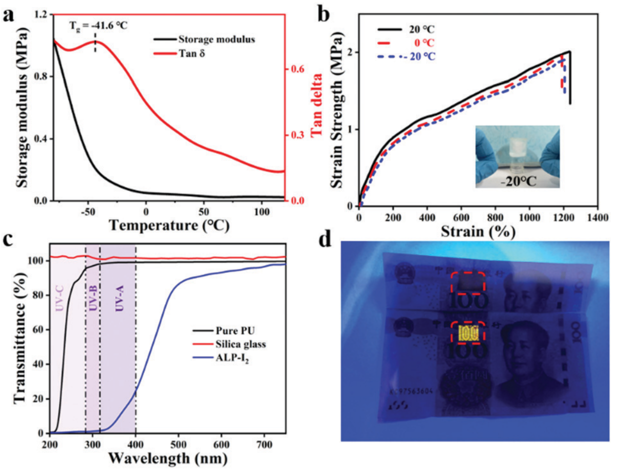

Fig. 6 Characterizations of the ionogel: (a) DMA of the ionogel; (b) strain properties of the ionogel at different temperatures, the insert picture is the stretched ionogel at −20 °C for 1 day storage; (c) the UV absorption of the ionogel; (d) demonstration of the remarkable UV-blocking performance of the ionogel.

The spectrum in the range of 320–400 nm (UV-A, ultraviolet spectrum) is believed to be the most harmful to human skin. Therefore, as an ionic skin, it is better to provide excellent UV-blocking properties. The UV absorption and resistance capability of the ionogel prepared in this study can be conferred by the abundant aromatic ring of the lignin. The UV-Vis transmittance tests were exploited to determine the UV-shielding ability of the ionogel ranging from 200 to 800 nm. As shown in Fig. 6c, the sample (ALP-I_2) shows excellent UV absorption (from 200 to 400 nm), the transmittances of the samples declined to 98.5% (PU) and 11.2% (ALP-I_2) in the range of UV-A, respectively. More importantly, the ionogel was subjected to be attached on the surface of banknote under UV-light to further demonstrate the UV-shielding capability. As shown in Fig. 6d, anti-counterfeit markings of the banknotes are selected for the experiment. The areas were attached with PU and ALP-I_2, respectively, donated as a control group and experimental group. It can be intuitively observed that the anti-counterfeiting logo appears in the control group, while the experimental group is the same as the original after the UV irradiation. The above results demonstrate the excellent UV filtering ability of the obtained ionogels.

Since ALP-I_2 contains a large number of positive imidazole ion groups and silver ions (Ag-Lignin NPs), the prepared ionogel should present excellent anti-bacterial properties. As a result, the anti-bacterial property of ionogel was investigated by testing the contact killing efficiencies (Gram-negative Escherichia coli (*E. coli*) and Gram-positive Staphylococcus aureus (*S. aureus*) as the representative bacteria). As presented in Fig. 7a and b, the killing efficiencies of ALP-I_2 against two bacterial strains are all higher than 95% after 1 h incubation, indicating excellent and broad-spectrum anti-bacterial ability. The SEM was further utilized to observe the shapes of the bacteria. As shown in Fig. 7c and d, all bacteria co-cultured with PU remained morphologically intact, while the bacteria co-cultured with ALP-I_2 underwent crumpling or cell membrane rupture, demonstrating the effective antibacterial properties of ALP-I_2. The mechanism of anti-bacterial activity for ALP-I_2 could be mainly attributed to the cationic imidazole ring and Ag-Lignin NPs. The microbial cell membranes would be electrostatically interacted by the cationic imidazole ring, which could lead to the leakage of the intracellular substances and ultimately to death. In addition, the anti-bacterial mechanism has already been well proved.[31,32] The Ag NPs can bind to the bacterial membrane and then enter the bacterium, deactivating the respiratory enzymes of the bacteria, blocking their respiration and eventually suffocating them. The killing efficiencies of PU against two bacterial strains are nearly the same as control group. Such results imply that the ionogel features excellent anti-microbial properties due to the synergistic effect of silver ions and ILs.

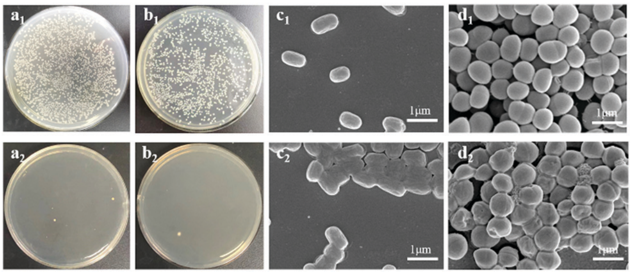

Fig. 7 Characterizations of antibacterial ability: (a and b) two kinds adhered viable bacterial of pure PU and ionogel against *E. coli* and *S. aureus*; (c and d) SEM photos of *E. coli* and *S. aureus* after incubating with pure PU and ionogel.

As a material that contacts intimately with the skin, it should not only have anti-bacterial properties, but also non-cytotoxic ones, otherwise it will cause harm to human skin in subsequent applications. The CCK-8 test with the cell line of HaCaT was used to measure the cytocompatibility of ionogel. After being incubated with the extracts of the ionogels, the cell viability of the ionogel group and the control group are higher than 79%. The results are better than the required cytotoxic standard of GB/T 16886.5-2017 and ISO 10993-5:2009, which demand no less than 70% (Fig. S4, ESI†).

All the above series of results indicate that the prepared ionogel has excellent performance of anti-freezing, UV-shielding, and anti-bacterial. Furthermore, the ionogel is no significant toxicity to cells.

High performance of ionogel strain sensors

Owing to the excellent conductivity of the ILs (Fig. S5, ESI†), the fabricated stretchable ionogel can be exploited as a strain sensor with high sensitivity. The sensing principle of the ionogel-based strain sensor depends mainly on the variation of the ion concentration per unit volume and the variation of the conductive path length during the deformation process. As exhibited in Fig. 8a, the resistance change of the sensor increases as it is gradually stretched. The Gauge factor (GF) is then calculated by the ratio of relative change in electrical resistance R to the mechanical strain ε $\left(\mathrm{GF} = \frac{(R - R_0)/R_0}{\varepsilon}\right)$. The GF for the ionogel sensor exhibits three near-linear regions with different slopes as the strain varied from 0% to 500% (Fig. 8a). As presented in Fig. 8b–d, the resistance change exhibited different variations under different stretching conditions. Interestingly, the obtained ionogel sensor demonstrates excellent stability by maintaining nearly identical sensing performance to the original sample after 100 cycles at 300% strain (Fig. 8e). Due to the ionogel having a T_g of -41.6 °C and remaining flexible at -20 °C, the ionogel is supposed to exhibit stable sensing performance at low temperatures as a strain sensor. As shown in Fig. 8f, the ionogel exhibits excellent ionic conductivities at low temperatures. Thus, the sensing performances of the ionogel at different temperatures and stored for different time periods at -20 °C were compared. As shown in Fig. 8g, the ionogel presents almost the same resistance change from -20 °C to 20 °C. When the ionogel was stored at -20 °C for various time periods, it demonstrates almost uniform resistance changes, and the sensing performance remains stable after multiple cycles (Fig. 8h). The sensing performance

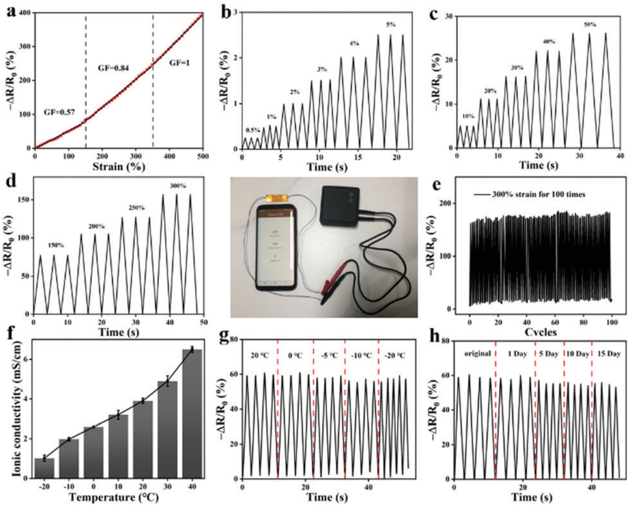

Fig. 8 The sensing performance of ionogel: (a) the variation of $\Delta R/R_0$ against the strain (gauge factor); the variation of $\Delta R/R_0$ at (b) 0.5% to 5%; (c) 5% to 50%; (d) 150% to 300%; (e) 300% for 100 cycles; (f) the conductivities of ionogel at different temperatures; the comparison of the sensing signal at (g) different temperatures; (h) different storage time periods at −20 °C.

of the ionogel sensor after self healing is also well maintained (Fig. S6, ESI†).

All the results discussed above indicate that the obtained ionogel sensor can provide reliable sensing performance under different conditions. Owing to the wide working range, and excellent mechanical, adhesion, and sensing properties of ionogel sensors, the feasibility of the ionogel sensor as a wearable sensor was discussed for diverse human motions. The ionogel is attached to the surface of human skin, and then the sensing signal is transmitted to the mobile device (smart phone or watch) in real-time *via* a bluetooth device, thus realizing the real-time monitoring of the human movement status.

Fig. 9 illustrates that the ionogel sensor was used to monitor the volunteer's movements. Owing to the sensitive sensing performance, the ionogel can detect the small movements of the human body. As shown in Fig. 9a, the ionogel is attached between the eyebrows, and when the volunteer frowns, a corresponding electrical signal appears in the app. When the ionogel is pressed firmly against the throat, the app also displays a different electrical signal as the volunteer makes a ha-ha-ha laugh (Fig. 9b). In addition, when the ionogel is affixed to detect the pulse, the app presents two unique electrical signals in the excited and resting states of the volunteer (Fig. 9c). Apart from detecting small physiological signals of the human body, this sensor can still detect large movements. As the finger and elbow are repeatedly bent, the relative resistance change of the sensor is clear and stable under different states (Fig. 9d and e). Similarly, the ionogel sensor is also attached to the knee to monitor the movement of the leg. As presented in Fig. 9f, once the body is in motion, the relative resistance changes immediately and noticeably. No observable baseline drift in the signal curve can be observed throughout the process of monitoring human movement. The ionogel sensors will offer many possibilities for smart wearable devices based on the stable and accurate reliability performance.

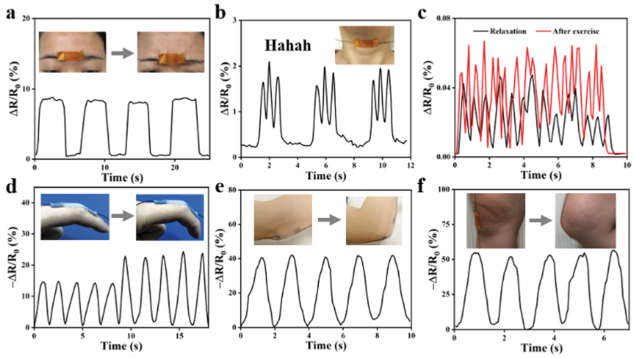

Fig. 9 Detection of human physiological signals: (a) frown; (b) say Hahaha; (c) pulse at relaxation and exciting; (d) finger; (e) elbow; (f) knee.

Conclusion

In summary, we have reported a multifunctional ionogel with exceptional mechanical properties, electrical conductivity, antimicrobial properties, and UV absorption properties. The ionogel also can be used as a reliable sensor with high sensitivity for sensing a wide range of strains. Some of the results obtained in this study present a new perspective for the design of novel multifunctional strain sensor, which will considerably broaden the application field of ionogels. There is no doubt that the ingeniously designed ionogel will be a significant inspiration for the next generation of artificial intelligence, wearable devices, and flexible robots.

Conflicts of interest

There are no conflicts to declare.

Acknowledgements

This work was funded by National Natural Science Foundation of China (NO. 51773129), Support Plan of Science and Technology Department of Sichuan Province, China (22ZDYF3307), International Science and Technology Cooperation Program of Chengdu (2020-GH02-00009-HZ), the Opening Project of Key Laboratory of Leather Chemistry and Engineering, (Sichuan University), Ministry of Education (SCU2021D005). The authors would thank Zhonghui Wang for her great help in FT-IR/SEM analyzer observation. We also appreciate Mi Zhou and Sha Deng for her assistance with the experimental test.

Notes and references

1 J.-Y. Sun, C. Keplinger, G. M. Whitesides and Z. Suo, *Adv. Mater.*, 2014, **26**, 7608–7614.

2 Z. Lei, Q. Wang, S. Sun, W. Zhu and P. Wu, *Adv. Mater.*, 2017, **29**, 1700321.

3 Z. Liu, Y. Wang, Y. Ren, G. Jin, C. Zhang, W. Chen and F. Yan, *Mater. Horiz.*, 2020, **7**, 919–927.

4 Y. Cao, Y. J. Tan, S. Li, W. W. Lee, H. Guo, Y. Cai, C. Wang and B. C. K. Tee, *Nat. Electron.*, 2019, **2**, 75–82.

5 T. Su, M. Zhang, Q. Zeng, W. Pan, Y. Huang, Y. Qian, W. Dong, X. Qi and J. Shen, *Bioact. Mater.*, 2021, **6**, 579–588.

6 Q. Zeng, Y. Qian, Y. Huang, F. Ding, X. Qi and J. Shen, *Bioact. Mater.*, 2021, **6**, 2647–2657.

7 J. Le Bideau, L. Viau and A. Vioux, *Chem. Soc. Rev.*, 2011, **40**, 907–925.

8 Y. Jian, S. Handschuh-Wang, J. Zhang, W. Lu, X. Zhou and T. Chen, *Mater. Horiz.*, 2021, **8**, 351–369.

9 Y. Liang, H. Li, L. Fan, R. Li, Y. Cui, X. Ji, H. Xiao, J. Hu and L. Wang, *Colloids Surf., A*, 2022, **633**, 127797.

10 T. Li, Y. Wang, S. Li, X. Liu and J. Sun, *Adv. Mater.*, 2020, **32**, 2002706.

11 J. Xu, H. Wang, X. Du, X. Cheng, Z. Du and H. Wang, *Chem. Eng. J.*, 2021, **426**, 130724.

12 T. Li, Y. Wang, S. Li, X. Liu and J. Sun, *Adv. Mater.*, 2020, **32**, 2002706.

13 B. Li, L. Kan, C. Li, W. Li, Y. Zhang, R. Li, H. Wei, X. Zhang and N. Ma, *J. Mater. Chem. C*, 2021, **9**, 1044–1050.

14 C. Chen, W. B. Ying, J. Li, Z. Kong, F. Li, H. Hu, Y. Tian, D. H. Kim, R. Zhang and J. Zhu, *Adv. Funct. Mater.*, 2022, **32**, 2106341.

15 L. Chen and M. Guo, *ACS Appl. Mater. Interfaces*, 2021, **13**, 25365–25373.

16 W. Liu, C. Fang, S. Wang, J. Huang and X. Qiu, *Macromolecules*, 2019, **52**, 6474–6484.

17 Y. Jia, L. Zhang, M. Qin, Y. Li, S. Gu, Q. Guan and Z. You, *Chem. Eng. J.*, 2022, **430**, 133081.

18 S. Kim and H. Chung, *ACS Sustainable Chem. Eng.*, 2021, **9**, 14766–14776.

19 J. Xu, H. Wang, X. Du, X. Cheng, Z. Du and H. Wang, *Chem. Eng. J.*, 2021, **426**, 130724.

20 Y. Fang, J. Xu, F. Gao, X. Du, Z. Du, X. Cheng and H. Wang, *Composites, Part B*, 2021, **219**, 108965.

21 N. Sun, Z. Wang, X. Ma, K. Zhang, Z. Wang, Z. Guo, Y. Chen, L. Sun, W. Lu, Y. Liu and M. Di, *Ind. Crops Prod.*, 2021, **174**, 114178.

22 P.-P. Jiang, H. Qin, J. Dai, S.-H. Yu and H.-P. Cong, *Nano Lett.*, 2021, DOI: 10.1021/acs.nanolett.1c03618.

23 W. Kong, Y. Yang, Y. Wang, H. Cheng, P. Yan, L. Huang, J. Ning, F. Zeng, X. Cai and M. Wang, *J. Mater. Chem. A*, 2022, **10**, 2012–2020.

24 Y. Chen, Y. Zhang, A. Mensaha, D. Li, Q. Wang and Q. Wei, *Carbohydr. Polym.*, 2021, **255**, 117508.

25 Q. Wang, X. Pan, C. Lin, X. Ma, S. Cao and Y. Ni, *Chem. Eng. J.*, 2020, **396**, 125341.

26 D. Sun, N. Li, J. Rao, S. Jia, Z. Su, X. Hao and F. Peng, *J. Mater. Chem. A*, 2021, **9**, 14381–14391.

27 Q. Wang, J. Guo, X. Lu, X. Ma, S. Cao, X. Pan and Y. Ni, *Int. J. Biol. Macromol.*, 2021, **181**, 45–50.

28 D. Gan, T. Shuai, X. Wang, Z. Huang, F. Ren, L. Fang, K. Wang, C. Xie and X. Lu, *Nano-Micro Lett.*, 2020, **12**, 169.

29 Z. Jia, X. Lv, Y. Hou, K. Wang, F. Ren, D. Xu, Q. Wang, K. Fan, C. Xie and X. Lu, *Bioact. Mater.*, 2021, **6**, 2676–2687.

30 D. Gan, W. Xing, L. Jiang, J. Fang, C. Zhao, F. Ren, L. Fang, K. Wang and X. Lu, *Nat. Commun.*, 2019, **10**, 1487.

31 W. Yang, F. Xu, X. Ma, J. Guo, C. Li, S. Shen, D. Puglia, J. Chen, P. Xu, J. Kenny and P. Ma, *Mater. Sci. Eng., C*, 2021, **129**, 112385.

32 S. Chernousova and M. Epple, *Angew. Chem., Int. Ed.*, 2013, **52**, 1636–1653.